ACS Catalysis
Letter
pubs.acs.org/acscatalysis

Iridium−Ruthenium Alloyed Nanoparticles for the Ethanol Oxidation Fuel Cell Reactions

Wenxin Du,[†] Nathaniel A. Deskins,[‡] Dong Su,[§] and Xiaowei Teng*,[†]

[†]Department of Chemical Engineering, University of New Hampshire, Durham, New Hampshire 03824, United States
[‡]Department of Chemical Engineering, Worcester Polytechnic Institute, Worcester, Massachusetts 01609, United States
[§]Center for Functional Nanomaterials, Brookhaven National Laboratory, Upton, New York 11973, United States

S *Supporting Information*

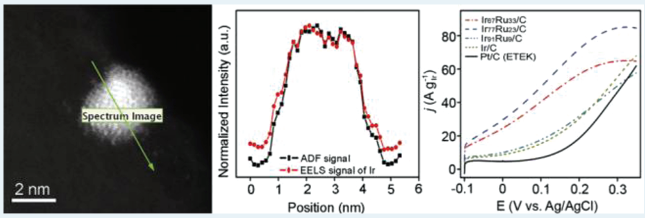

ABSTRACT: In this study, carbon supported Ir−Ru nanoparticles with average sizes ranging from 2.9 to 3.7 nm were prepared using a polyol method. The combined characterization techniques, that is, scanning transmission electron microscopy equipped with electron energy loss spectroscopy, high resolution transmission electron microscopy, energy dispersive X-ray spectroscopy, and X-ray diffraction, were used to determine an Ir−Ru alloy nanostructure. Both cyclic voltammetry and chronoamperometry (CA) results demonstrate that $Ir_{77}Ru_{23}/C$ bears superior catalytic activities for the ethanol oxidation reaction compared to Ir/C and commercial Pt/C catalysts. In particular, the $Ir_{77}Ru_{23}/C$ catalyst shows more than 21 times higher mass current density than that of Pt/C after 2 h reaction at a potential of 0.2 V vs Ag/AgCl in CA measurement. Density functional theory simulations also demonstrate the superiority of Ir−Ru alloys compared to Ir for the ethanol oxidation reaction.

KEYWORDS: *Ir−Ru nanoparticle, alloy, ethanol oxidation reaction, DFT calculations*

Direct ethanol fuel cells (DEFCs) have attracted much attention as a renewable energy source for both portable and stationary electronic applications because of several unique characteristics of ethanol fuel such as availability from biomass production, low toxicity, and safety for storage and transportation in liquid form.[1−3] Although ethanol may be considered a promising and productive fuel for fuel cell reactions, research and development of DEFC technology has been hindered by the lack of cost-effective anode catalysts. Platinum (Pt)-based nanostructured materials have commonly been used as excellent anode catalysts for electro-oxidation of small organic molecules (SOMs) because of the high catalytic activity of Pt for dissociation of SOMs. Ethanol oxidation reaction (EOR) is a complex twelve-electron transfer reaction, which involves various reaction intermediates such as acetaldehyde, acetic acid, carbon monoxide, and other dehydrogenation fragments.[4,5] These strongly adsorbed reaction intermediates, CO in particular, can block active sites on the surface Pt and exacerbate the charge transfer considerably. Also, the high expense of Pt metal has seriously restricted their implementation for commercial application.

Several notable theoretical and experimental efforts have gone into developing active effective catalysts with high activity and selectivity toward the EOR.[6−15] Mavrikakis, Nørskov, and co-workers recently reported that several Platinum Group Metals (PGMs) including Pt, Pd, Ir, Rh, and Ru could decompose ethanol effectively using both experimental and theoretical methods.[16] Among these five PGMs, catalysts containing Pt, Pd, Rh, and Ru have been well demonstrated for the EOR. However, Ir-based electrocatalysts have only been reported in limited studies for the oxygen reduction reaction and oxidation of SOMs.[8,17−21] Recently, experimental and theoretical efforts from our group found the highly active Ir−Sn heterogeneous nanocatalysts for the EOR, strongly demonstrating the potential of Ir metal as an alternative catalyst in fuel cell reactions because of their favorable properties in dissociating SOMs compared to Pt.[12] Although Pt−Ru has been considered as one of the best binary catalysts for the electro-oxidation of SOMs, its Ir-based counterpart (Ir−Ru) has not been reported to our knowledge. Questions, including the optimum atomic ratio between Ir and Ru, and alloying effect of Ir−Ru for the EOR, still remain. In this paper, we show the synthesis and structure characterizations of carbon supported Ir−Ru alloyed electrocatalysts. Their catalytic performance toward EOR has been measured and estimated using electrochemical techniques and density functional theory (DFT) calculations.

Ir−Ru nanoparticles were prepared by a polyol approach using hydrous $IrCl_3 \cdot xH_2O$ (Alfa Aesar, 99.9%) and $RuCl_3 \cdot xH_2O$ (Alfa Aesar, 99.9%) as precursors at 170 °C using ethylene glycol (EG) as solvent/reducing agent and polyvinylpyrrolidone (PVP) as stabilizing agent. The resulting particles were then mixed with active carbon (Vulcan, XC-72R), and treated at 300 °C in air followed by H_2 flow at 100

Received: April 8, 2012
Revised: May 13, 2012
Published: May 14, 2012

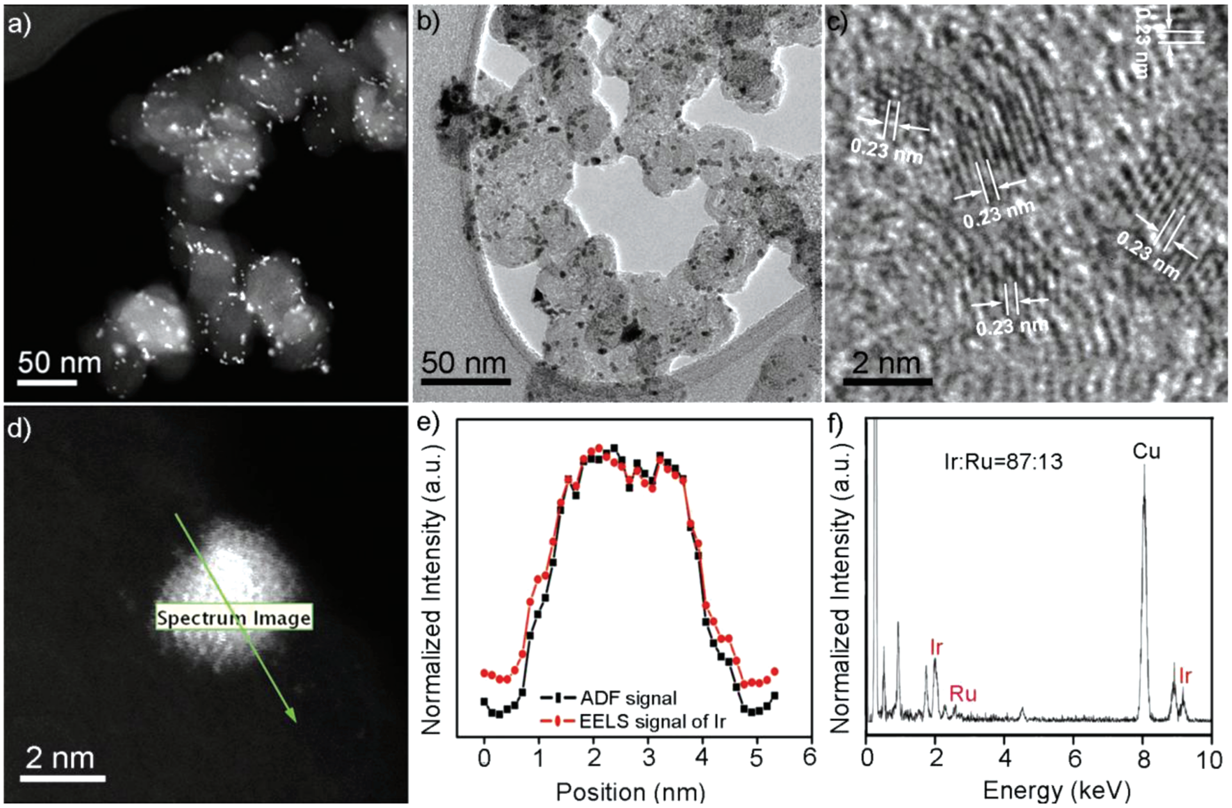

Figure 1. (a) HAADF image, (b) bright field TEM image, and (c) HRTEM of carbon supported $Ir_{77}Ru_{23}$ nanoparticles, and (d) HAADF image, (e) ADF and EELS line scans, and (f) EDS probing of an individual $Ir_{77}Ru_{23}$ nanoparticle.

°C (see a detailed experimental procedure in Supporting Information). The nominal metal loadings (Ir and Ru) on carbon for all these Ir−Ru samples were 15 wt %. High−angle angular dark−field (HAADF) scanning transmission electron microscopy (STEM) was performed using aberration-corrected Hitachi HD 2700C at the Center for Functional Nanomaterials at the Brookhaven National Laboratory. Figures 1a and 1b show HAADF and bright field images of large-area carbon supported Ir−Ru nanoparticles, where the particles were evenly dispersed throughout the carbon support. The chemical composition of a large area (around 50 × 50 μm) of Ir−Ru catalyst was determined to be $Ir_{77}Ru_{23}$ using energy dispersive X-ray spectroscopy (EDS) (Supporting Information, Figure S1). The average size of $Ir_{77}Ru_{23}$ was calculated to be 3.7 ± 0.8 nm with a relatively narrow size distribution after analyzing over 250 particles (Supporting Information, Figure S2). The HRTEM of $Ir_{77}Ru_{23}$ nanoparticles shown in Figure 1c clearly demonstrates the well-defined crystalline structure. The distances between adjacent fringes were calculated to be ~0.23 nm, which could be attributed to (111) planes of Ir or Ir-based alloys.

Figures 1d and 1e show the HAADF image of a single particle of $Ir_{77}Ru_{23}$, and annular dark field (ADF) and EELS line scans as functions of mapping distance. Both ADF and EELS profiles show a typical "volcano" shape concurrently, indicating a nearly homogeneous distribution of Ir atoms within the individual particle. Similar profiles of Ir were also observed from different Ir−Sn particles (Supporting Information, Figure S3). The ADF and EELS spectra of Ru atoms were not available. The difficulty of detecting Ru might be attributed to the interference of carbon K edge under EELS mode. Instead, EDS probing was used as an alternative to analyze the chemical composition of single $Ir_{77}Ru_{23}$ particles. The EDS spectrum in Figure 1f evidenced the presence of Ru within the particle, and the molar percentage of Ru was determined to be around 13%. We note that the Ru ratio detected by single-particle EDS probing using STEM is relatively lower than that by large area EDS equipped on SEM (13% vs 23%). The discrepancy between the two techniques could be attributed to (i) particle-to-particle deviation of the Ru composition, or (ii) the smaller atomic number of Ru atoms make its EDS signal harder to be collected in single-particle probing, whereas limited data acquisition time was applied to prevent the damage of the particles.

By varying the ratios between Ir and Ru metal precursors during the synthesis (see Supporting Information for details), we also prepared two other carbon supported Ir−Ru nanoparticles, that is, $Ir_{67}Ru_{33}$ and $Ir_{91}Ru_{9}$, of which the compositions were verified by EDS. As we can see from Supporting Information, Figure S4, both Ir−Ru nanoparticles are evenly distributed throughout carbon support in TEM with average sizes of 2.9 ± 0.7 and 2.9 ± 0.9 nm, respectively. X-ray diffraction (XRD) was used to analyze the crystalline structure of carbon supported Ir−Ru nanoparticles as shown in Figure 2. The relatively broad peak around 25° can be attributed to the carbon black (002) planes. All the Ir−Ru/C binary catalysts showed a face-centered-cubic (fcc) crystalline structure with (111), (200), and (220) indexed planes, analogous to those in an Ir/C catalyst made by a similar approach. The Ir−Ru/C catalysts with different chemical compositions showed right-shifted diffraction peaks compared to Ir/C, which can be explained by the contracted lattice of Ir upon the alloying with the Ru atoms which have relatively smaller atomic size. In particular, the $Ir_{77}Ru_{23}/C$ and $Ir_{67}Ru_{33}/C$ showed more

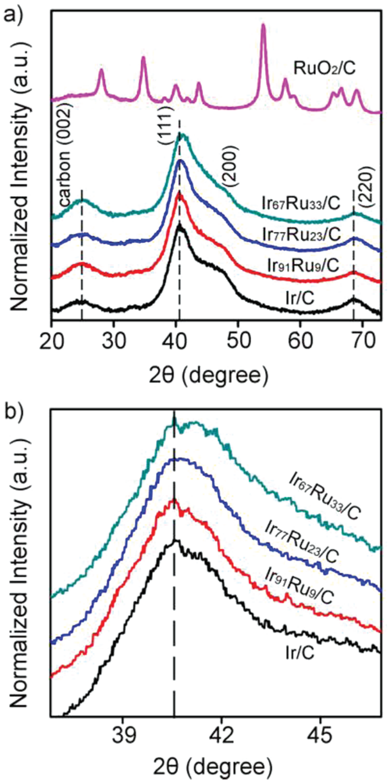

Figure 2. XRD patterns of carbon supported $Ir_{67}Ru_{33}$, $Ir_{77}Ru_{23}$, $Ir_{91}Ru_9$, and Ir nanoparticles.

noticeable peak shifting, that is, ~0.2 and ~0.4 degrees higher than that of Ir/C for the (111) peak, respectively. Complementary data from a STEM line scan of Ir (Figure 1e), single particle EDS probing of Ir/Ru spectra (Figure 1f), as well as the peak-shifted XRD spectra of Ir–Ru compared to that of pure Ir (Figure 2), unambiguously demonstrated the alloy formation between Ir and Ru. In addition, no diffraction peaks from RuO_2 can be discerned in the $Ir_{77}Ru_{23}/C$ sample compared to an XRD pattern of rutile type of RuO_2 synthesized via a similar approach, indicating the dominance of alloy phase in IrRu/C catalyst. To calculate the average size of Ir–Ru/C, Scherrer's equation was employed. The $Ir_{77}Ru_{23}$ particles only showed an average diameter of 2.0 nm (see Table 1), which is substantially smaller than the size calculated from TEM images (3.7 ± 0.8 nm). This size discrepancy may be due to the partial agglomeration from individual $Ir_{77}Ru_{23}$ crystals (as readily seen from Figure 1), which were counted as a whole particle in TEM, thus increasing the overall size of particles. We note that maximum Ru content for the Ir–Ru system is 33%. When more Ru precursors were used, a segregated RuO_2 phase appeared, indicating the formation of Ir–Ru alloy and RuO_2 mixed phases.

The electrochemical activities for the EOR of $Ir_{77}Ru_{23}/C$ were evaluated through cyclic voltammetry (CV) and chronoammerometry (CA) measurements. All the potentials reported here are referenced to Ag/AgCl (1 M KCl). The CV measurements of Ir–Ru/C catalysts in 0.5 M H_2SO_4 are shown in Supporting Information, Figure S5, whereas hydrogen adsorption features between potentials −0.217 and 0.06 V were used to calculate the electrochemical surface area (ECSA). A columbic charge of 220 $\mu C\ cm^{-2}$ was used to calculate the value of ECSA in Ir–Ru catalysts, because of the similar interactions between Pt/H and Ir/H.[22,23] Figure 3a shows the polarization curve of Ir–Ru/C in comparison with Ir/C and commercial Pt/C (ETEK, 20%) in an electrolyte containing 0.5 M H_2SO_4 and 0.5 M ethanol. The mass current density of $Ir_{77}Ru_{23}/C$ averaged by Ir mass was significantly higher than that of Ir/C and commercial Pt/C all over the potential range of −0.1 to 0.35 V in CV measurement. At the voltage of 0.2 V, the mass current density of $Ir_{77}Ru_{23}/C$ is 2.4 times and 3.9 times higher than that of Ir/C and Pt/C (ETEK), respectively. Note that although a rotation disk electrode was used for all the electrochemical measurements, we believe that the EOR in half-cell measurements is not mass-transfer limited: When rotation (1000 rpm) was applied, $Ir_{77}Ru_{23}$ showed only marginally higher current density (less than 5%) compared to that under zero rotation (Supporting Information, Figure S6).

The superior performance of $Ir_{77}Ru_{23}/C$ toward EOR was also demonstrated in CA measurements as shown in Figure 3b, conducted at a constant voltage of 0.2 V. The $Ir_{77}Ru_{23}/C$ exhibits superior activity with a mass current density of 5.2 A g^{-1} (with respective to the mass of Ir) after 2 h reaction, while Ir/C and commercial Pt/C only retained mass current densities of 1.7 A g^{-1} and 0.24 A g^{-1} (respective to the mass of Pt), respectively. $Ir_{77}Ru_{23}/C$ shows more than 3 times and 21 times higher mass current density than Ir/C and Pt/C (ETEK) after 2 h of reaction. The specific current density averaged by ECSA in CV and CA measurements also showed a similar trend (see Table 1). Although the $Ir_{67}Ru_{33}/C$ displayed an inferior electroactivity to $Ir_{77}Ru_{23}/C$ in EOR, it outperformed Ir/C and Pt/C (ETEK) in CV and CA measurements. The $Ir_{91}Ru_9/C$ behaves alike Ir/C in EOR: it shows slightly inferior current density than Ir/C during a potential sweep of 0.25 to 0.35 V in CV but

Table 1. Results Obtained for Ethanol Electro-Oxidation on Different Ir–Ru Catalysts

					CV		CA	
catalysts	TEM size (nm)	XRD size (nm)	ECSA (cm^2)[a]	mass loading of Ir or Pt (μg)	j at 0.2 V (A g^{-1})[b]	j at 0.2 V ($\mu A\ cm^{-2}$)[b]	j at 0.2 V at 2 h (A g^{-1})[c]	j at 0.2 V at 2 h ($\mu A\ cm^{-2}$)[c]
Pt/C (ETEK)	N/A	2.7	2.09	2.5	18.5	22.2	0.24	0.3
$Pt_{50}Ru_{50}/C$ (JM)	N/A	N/A	1.36	2.3	33.2	54.3	N/A	N/A
$Pt_{77}Sn_{23}/C$ (homemade)	4.3 ± 1.2	N/A	0.93	3.2	56.1	191.4	N/A	N/A
Ir/C	3.4 ± 1.1	2.2	1.45	3.8	30.3	78.2	1.7	4.7
$Ir_{91}Ru_9/C$	2.9 ± 0.9	1.9	1.68	3.6	31.7	67.5	2.4	5.1
$Ir_{77}Ru_{23}/C$	3.7 ± 0.8	2.0	1.86	3.3	72.0	111.8	5.2	8.3
$Ir_{67}Ru_{33}/C$	2.9 ± 0.7	2.1	1.48	3.0	52.2	105.7	4.2	8.5

[a] −0.217 V vs Ag/AgCl was arbitrarily chosen as boundary to calculate ECSAs of Ir based materials. [b] Mass and specific current density at 0.2 V in CV measurements. [c] Mass and specific current density after 2 h reaction in CA measurements.

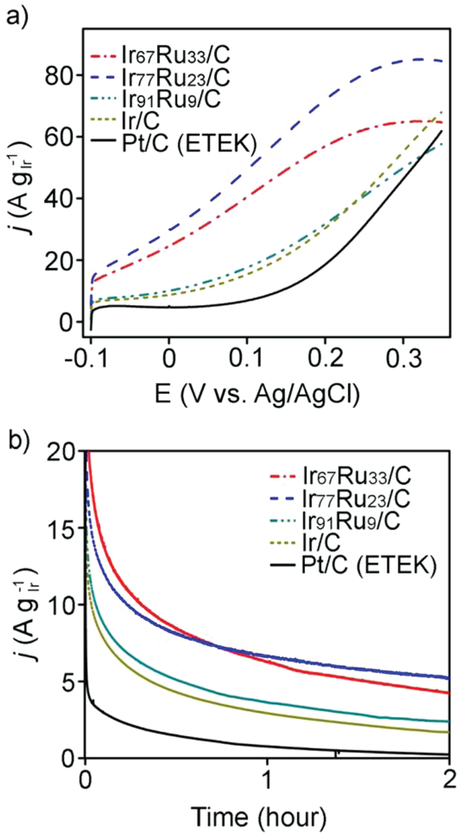

Figure 3. (a) Polarization curves and (b) chronoamperometric measurements of Ir−Ru/C in comparison with Ir/C and Pt/C (ETEK) at a potential of 0.2 V in 0.5 M H_2SO_4 + 0.5 M ethanol solutions at scan rate of 30 mV s^{-1} at room temperature. Both measurements were conducted using a rotating disk electrode at a rate of 1000 rpm.

40% higher quasi-steady state current density than that of Ir/C in CA measurement after 2 h of reaction. Long-term CA measurements (up to 10 h) were also conducted for $Ir_{77}Ru_{23}$/C and Pt/C (ETEK) catalysts. Supporting Information, Figure S7 shows that the current density of commercial Pt/C dropped to zero after 4.3 h of reaction, while $Ir_{77}Ru_{23}$ maintained a measurable current even after a 10 h period. Long-term CA measurements undoubtedly demonstrate the superior anti-poisoning ability of Ir−Ru catalysts compared to that of Pt.

Although results on Ir-based electrocatalysts have been rarely reported for the EOR, Pt-based materials have been intensively studied. In particular, the Pt−Sn system has been considered as one of the best anode catalysts for the EOR.[4,7] We have compared the electroactivities of $Ir_{77}Ru_{23}$/C with a commercial $Pt_{50}Ru_{50}$/C catalyst (Johnson Matthey Inc.) and a homemade $Pt_{77}Sn_{23}$/C catalyst as summarized in Table 1. CV data show that our $Ir_{77}Ru_{23}$ outperforms $Pt_{77}Sn_{23}$ and $Pt_{50}Ru_{50}$ at 0.2 V (vs Ag/AgCl) with a higher mass-specific current density. However, $Pt_{77}Sn_{23}$ catalysts showed around 70% higher current density averaged by ECSA, compared to $Ir_{77}Ru_{23}$ (Supporting Information, Figure S8 and Table 1). In addition to commercial $Pt_{50}Ru_{50}$/C and homemade $Pt_{77}Sn_{23}$/C catalysts, we also compared the electroactivities of $Ir_{77}Ru_{23}$/C with our recently reported $Ir_{71}Sn_{29}$/C catalysts for EOR (Supporting Information, Figure S8).[12] From the polarization curve, we can see that $Ir_{71}Sn_{29}$/C catalysts had much lower peak potential and higher peak current density compared to $Ir_{77}Ru_{23}$ catalysts (Supporting Information, Figure S8a). However, $Ir_{77}Ru_{23}$ showed much higher electrochemical stability: upon sweeping between −0.25 to 0.8 V in 0.5 M H_2SO_4 electrolyte, for $Ir_{77}Ru_{23}$/C 55% of the initial ECSA remained after 50 cycles of CVs, while for $Ir_{71}Sn_{29}$/C only 25% remained (Supporting Information, Figure S8b and S8c).

In a noble metal-transition metal binary system, higher transition metal (TM) content will generate more $TM{-}OH_{ads}$ complexes, resulting from the dissociative adsorption of water, which facilitate the oxidation of adsorbed SOMs. However, higher TM content will also decrease the occupancy of active noble metal atoms on the surface, and consequently impair the overall performance of dissociation of adsorbed SOMs. Therefore, an optimal composition usually exists as a result of such rival effects. The optimal ratio of Ru in Ir−Ru alloy for the electro-oxidation of SOMs has not been reported, while that of Ru in Pt−Ru binary system has been intensively studied with various controversial results, especially for the methanol oxidation reaction (MOR).[24,25] Watanabe, Loffler, and Gilman reported $Pt_{50}Ru_{50}$ alloy had the best performance in MOR,[26−28] while Gasteiger et al. found that for the MOR, the optimal Ru content on the surface of polycrystalline Pt−Ru bulk alloys had strong temperature-dependency: ∼10% and ∼30% surface Ru were the optimal ratios at 25 and 60 °C, respectively.[29,30] They also proposed that the surface enrichment of Pt could be responsible for controversial results on the optimal Ru ratios in Pt−Ru systems, which was largely ignored by previous studies. Similarly, Iwasta and Abruna found a broad maximum in activity for MOR between 10 to 40% of surface Ru for Pt−Ru alloy at room temperature.[31,32] Furthermore, Cuesta studied the cyanide-modified Pt(111) electrodes for MOR,[33] and found out that an ensemble of three contiguous Pt atoms was indispensible for CO formation through dehydrogenation of methanol, strongly indicating Pt_3Ru_1 might be the perfect surface composition to mitigate the CO poisoning, which is consistent with above-reported results for MOR. In the present work, Ir_{77}−Ru_{23} nanoparticles showed the highest catalytic activity for EOR. Although the surface composition of Ru is unknown in this report, it is expected that surface composition should not differ significantly from bulk composition. This is because the surface enrichment of Ir is less severe compared to Pt in Pt−Ru system, as the surface free energy of Ir is analogous to that of Ru (3.231 J m^{-2} vs 3.409 J m^{-2}) at 25 °C.[6,34,35] The optimal ratio between Ir and Ru is close to ∼3:1, indicating that an ensemble of three contiguous of Ir atoms might be also necessary for the EOR, during which removal of strongly adsorbed CO might be crucial.

Previous in situ differential electrochemical mass spectrometry and Fourier transform infrared spectroscopy studies showed that the selectivity for complete oxidation of ethanol into CO_2 via C−C cleavage is low.[5,13,14,31,36,37] Even using the best Pt_3Sn_1 catalysts less than 5% of ethanol can be oxidized into CO_2 at room temperature in an acid medium, with the major products being acetaldehyde and acetic acid.[38] Therefore, studying and developing anode catalysts for complete oxidation of ethanol into CO_2 to achieve a twelve-electron transfer remain a challenge. To assess the ability of Ir−Ru for C−C cleavage during the EOR, CVs and CA of $Ir_{77}Ru_{23}$/C and Pt/C in the presence of ethanol, acetaldehyde, and acetic acid are compared as shown in Supporting Information, Figure S9. Polarization curves in Supporting Information, Figure S9 (a, b and c) indicated that (i) both $Ir_{77}Ru_{23}$/C and Pt/C catalysts were active toward the oxidation of ethanol and acetaldehyde.

The current densities in acetic acid oxidation only appeared as background current (i.e., CV current in H_2SO_4-only electrolyte), suggesting no acetic acid was oxidized on the surface of Pt or Ir−Ru; (ii) for each fuel, $Ir_{77}Ru_{23}$/C appeared to have a higher current density, indicating better electroactivity of $Ir_{77}Ru_{23}$/C toward dissociation of SOMs compared to Pt/C. Meanwhile, CAs in Supporting Information, Figure S9 (d and e) show that (i) there were no noticeable CA currents found in $Ir_{77}Ru_{23}$/C and Pt/C when using acetic acid as a fuel; (ii) $Ir_{77}Ru_{23}$/C exhibited higher current densities compared to Pt/C; after 6000 s CA measurements, $Ir_{77}Ru_{23}$/C showed current densities of 0.05 A/g and 5.6 A/g in the presence of acetaldehyde and ethanol, respectively. During the EOR, formation of acetaldehyde and acetic acid would deliver two and four electrons, respectively. A 112 times increase of the current density in CA for $Ir_{77}Ru_{23}$/C observed by using ethanol over acetaldehyde as fuels strongly indicated a certain amount of C−C scission happened when using ethanol as a fuel, to deliver more than a four-electron charge transfer reaction. We notice that about a 40 times increase of the current density observed from Pt/C when using acetaldehyde and ethanol (0.01 A/g vs 0.4 A/g), respectively. These data also indicate $Ir_{77}Ru_{23}$/C might exhibit a better C−C cleavage ability compared to Pt/C.

We used DFT simulations to assess the electroactivity of Ir, Pt, and Ir−Ru catalysts for EOR. We modeled (111) surfaces of Ir, Pt, and an Ir−Ru binary cluster as shown in Figure 4. In the binary cluster, the top layer of Ir atoms was replaced by Ru, giving an overlayer structure. Full details on the simulations are given in the Supporting Information. During ethanol oxidation, a large number of intermediates may form after C−H, C−O, or C−C bond scission. C−C bond scission is one the most difficult steps during ethanol oxidation, and previous DFT work[16,39] indicates the reaction $CHCO_{ads} \rightarrow CO_{ads} + CH_{ads}$ to be the most likely rate-determining step. Accordingly we modeled this reaction, as well as the reaction $CH_2CO_{ads} \rightarrow CO_{ads} + CH_{2\text{-}ads}$ over the Ir, Pt, and Ir−Ru surfaces.

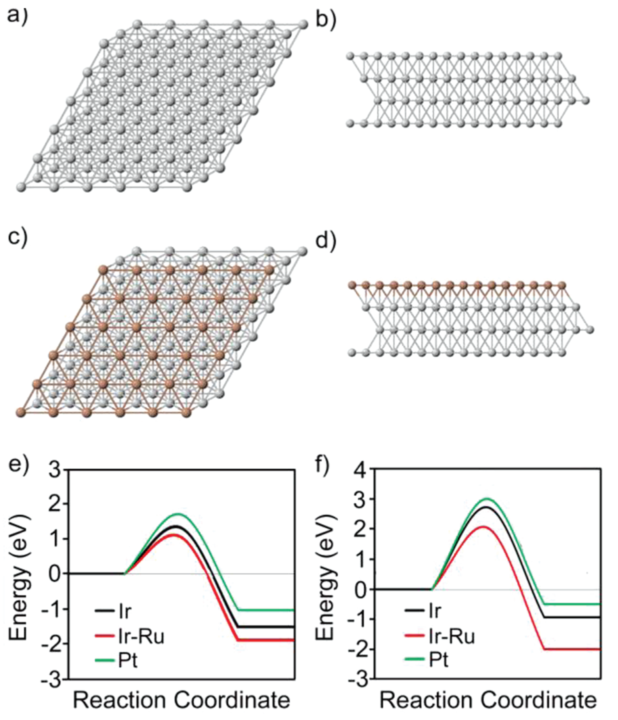

Figure 4. (a) Top and (b) side views of the Ir (111) slab used in the current work. The Pt (111) slab was equivalent. (c) Top and (d) side views of the Ir−Ru (111) slab used in the current work. Gray spheres represent Ir atoms and brown spheres represent Ru atoms. Calculated reaction energy diagram for C−C bond scission of (e) $CHCO_{ads}$ and (f) CH_2CO_{ads} over Ir, Pt, and Ir−Ru surfaces. Reactant states are adsorbed intermediates (CHCO and CH_2CO), and product states are adsorbed dissociated species (CH/CO and CH_2/CO). The transition state energy indicates the kinetic barrier for dissociation. The reference state (adsorbed reactant) on both surfaces was taken to be 0 eV.

Results from our calculations are shown in Figures 4e and 4f. For both reactants C−C bond breaking is easier (lower reaction barrier) over the Ir−Ru alloy surface, supporting our experimental results that Ru alloying with Ir leads to a better catalyst. Scission of CHCO (Figure 4e) also has a lower barrier compared to CH_2CO (Figure 4f), indicating that C−C bond scission is more likely to proceed via a CHCO intermediate. As already mentioned, CHCO scission has been proposed as the rate-determining step,[16,39] and our results are in agreement with this. We mention that while we have only considered one potential alloy structure, our calculated activity trends for ethanol oxidation/decomposition are as follows: Ir−Ru > Ir > Pt. This fully supports the superiority of Ir−Ru alloy catalysts over Ir and Pt catalysts which we observed experimentally. In these calculations we assumed the C−C splitting of ethanol occurred relative to the gas phase on metallic surfaces, and ignored the effect of aqueous environment, or dielectric background. Although this is different from the realistic reaction environment, this simplified approach is often used as a starting point to understanding catalytic reactions under real-world conditions. DFT calculations in aqueous solution and under applied potentials may be considered in future work, especially the effects of dissociated water molecules and external potentials on the C−C scission of ethanol fuel.

In conclusion, carbon supported Ir−Ru nanoparticles with average sizes between 2.9 to 3.7 nm were prepared via a polyol process in the presence of PVP. Complementary characterization techniques including STEM equipped EELS line scan, HRTEM, single-particles EDS probing, and XRD revealed an Ir−Ru alloyed structure. The catalytic activities of Ir−Ru/C toward EOR were measured, and compared with Ir/C and commercial Pt/C (ETEK) by CV and CA measurements. $Ir_{77}Ru_{23}$/C was determined to be the optimal chemical composition for the EOR, which can be further attributed to the alloying effect between Ir and Ru. DFT calculations indicate the C−C bond scission during ethanol electro-oxidation is energetically more favorable on an Ir−Ru alloy catalyst compared to on an Ir and a Pt catalyst. Our study highlights the potential of Ir−Ru alloys as alternative electrocatalysts for DEFC applications. Future studies on Ir-based catalysts to further reduce its cost and enhance its electroactivity for EOR are needed.

■ ASSOCIATED CONTENT

Ⓢ Supporting Information

Detailed experimental procedures, large area EDS spectra of Ir−Ru/C nanoparticles, size distribution of carbon supported $Ir_{77}Ru_{23}$ nanoparticles, TEM of carbon supported $Ir_{67}Ru_{33}$, HAADF images and ADF plus EELS line scans of a individual $Ir_{77}Ru_{23}$ nanoparticle, $Ir_{91}Ru_9$, Ir and RuO_2 nanoparticles and CVs of Ir−Ru/C, $Ir_{71}Sn_{29}$, $Pt_{77}Sn_{23}$, $Pt_{50}Ru_{50}$ (JM) catalysts in 0.5 M H_2SO_4 electrolyte, details of DFT calculations. The CVs and CAs of $Ir_{77}Ru_{23}$/C and Pt/C using ethanol, acetaldehyde, and acetic acid as fuels are also included. This material is available free of charge via the Internet at http://pubs.acs.org.

■ AUTHOR INFORMATION

Corresponding Author

*E-mail: xw.teng@unh.edu.

Funding

This work is supported in part by the University of New Hampshire (X.T., W.D.). Research carried out in part at the Center for Functional Nanomaterials, Brookhaven National Laboratory, which is supported by the U.S. Department of Energy, Office of Basic Energy Sciences, under Contract No. DE-AC02-98CH10886.

Notes

The authors declare no competing financial interest.

■ ACKNOWLEDGMENTS

We thank Sia Najafi at WPI for help in using WPI's computer clusters, and we acknowledge Nancy Cherim at UNH for the assistance in TEM and EDS measurements.

■ REFERENCES

(1) Acres, G. J. K. *J. Power Sources* **2001**, *100*, 60−66.

(2) Lave, L. B.; Griffin, W. M.; MacLean, H. *Issues Sci. Technol.* **2001**, *18*, 73−78.

(3) Parsons, R.; Vandernoot, T. *J. Electroanal. Chem.* **1988**, *257*, 9−45.

(4) Lamy, C.; Belgsir, E. M.; Leger, J. M. *J. Appl. Electrochem.* **2001**, *31*, 799−809.

(5) Vigier, F.; Coutanceau, C.; Perrard, A.; Belgsir, E. M.; Lamy, C. *J. Appl. Electrochem.* **2004**, *34*, 439−446.

(6) Antolini, E. *Mater. Chem. Phys.* **2003**, *78*, 563−573.

(7) Antolini, E. *J. Power Sources* **2007**, *170*, 1−12.

(8) Cao, L.; Sun, G. Q.; Li, H. Q.; Xin, Q. *Electrochem. Commun.* **2007**, *9*, 2541−2546.

(9) Du, W. X.; Mackenzie, K. E.; Milano, D.; Deskins, N. A.; Su, D.; Teng, X. W. *ACS Catal.* **2012**, *2*, 287−297.

(10) Du, W. X.; Su, D.; Wang, Q.; Frenkel, A. I.; Teng, X. W. *Cryst. Growth Des.* **2011**, *11*, 594−599.

(11) Du, W. X.; Wang, Q.; LaScala, C. A.; Zhang, L. H.; Su, D.; Frenkel, A. I.; Mathur, V. K.; Teng, X. W. *J. Mater. Chem.* **2011**, *21*, 8887−8892.

(12) Du, W. X.; Wang, Q.; Saxner, D.; Deskins, N. A.; Su, D.; Krzanowski, J. E.; Frenkel, A. I.; Teng, X. W. *J. Am. Chem. Soc.* **2011**, *133*, 15172−15183.

(13) Kowal, A.; Li, M.; Shao, M.; Sasaki, K.; Vukmirovic, M. B.; Zhang, J.; Marinkovic, N. S.; Liu, P.; Frenkel, A. I.; Adzic, R. R. *Nat. Mater.* **2009**, *8*, 325−330.

(14) Li, M.; Kowal, A.; Sasaki, K.; Marinkovic, N.; Su, D.; Korach, E.; Liu, P.; Adzic, R. R. *Electrochim. Acta* **2010**, *55*, 4331−4338.

(15) Zhou, W. J.; Zhou, Z. H.; Song, S. Q.; Li, W. Z.; Sun, G. Q.; Tsiakaras, P.; Xin, Q. *Appl. Catal., B* **2003**, *46*, 273−285.

(16) Ferrin, P.; Simonetti, D.; Kandoi, S.; Kunkes, E.; Dumesic, J. A.; Norskov, J. K.; Mavrikakis, M. *J. Am. Chem. Soc.* **2009**, *131*, 5809−5815.

(17) Aramata, A.; Yamazaki, T.; Kunimatsu, K.; Enyo, M. *J. Phys. Chem.* **1987**, *91*, 2309−2314.

(18) Ioroi, T.; Yasuda, K. *J. Electrochem. Soc.* **2005**, *152*, A1917−A1924.

(19) Lee, K.; Zhang, L.; Zhang, J. J. *J. Power Sources* **2007**, *170*, 291−296.

(20) Lee, K.; Zhang, L.; Zhang, J. J. *J. Power Sources* **2007**, *165*, 108−113.

(21) Takasu, Y.; Yoshinaga, N.; Sugimoto, W. *Electrochem. Commun.* **2008**, *10*, 668−672.

(22) Gojkovic, S. L. *J. Electroanal. Chem.* **2004**, *573*, 271−276.

(23) Pajkossy, T.; Kibler, L. A.; Kolb, D. M. *J. Electroanal. Chem.* **2007**, *600*, 113−118.

(24) Arico, A. S.; Srinivasan, S.; Antonucci, V. *Fuel Cells* **2001**, *1*, 133−161.

(25) Petrii, O. A. *J. Solid State Electrochem.* **2008**, *12*, 609−642.

(26) Chu, D.; Gilman, S. *J. Electrochem. Soc.* **1996**, *143*, 1685−1690.

(27) Loffler, M. S.; Natter, H.; Hempelmann, R.; Wippermann, K. *Electrochim. Acta* **2003**, *48*, 3047−3051.

(28) Watanabe, M.; Uchida, M.; Motoo, S. *J. Electroanal. Chem.* **1987**, *229*, 395−406.

(29) Gasteiger, H. A.; Markovic, N.; Ross, P. N.; Cairns, E. J. *J. Phys. Chem.* **1993**, *97*, 12020−12029.

(30) Gasteiger, H. A.; Markovic, N.; Ross, P. N.; Cairns, E. J. *J. Electrochem. Soc.* **1994**, *141*, 1795−1803.

(31) Iwasita, T.; Hoster, H.; John-Anacker, A.; Lin, W. F.; Vielstich, W. *Langmuir* **2000**, *16*, 522−529.

(32) Wang, H. S.; Alden, L. R.; DiSalvo, F. J.; Abruna, H. D. *Langmuir* **2009**, *25*, 7725−7735.

(33) Cuesta, A. *J. Am. Chem. Soc.* **2006**, *128*, 13332−13333.

(34) Jeon, M. K.; Lee, K. R.; Jeon, H. J.; Woo, S. I. *J. Appl. Electrochem.* **2009**, *39*, 1503−1508.

(35) Mezey, L. Z.; Giber, J. *Jpn. J. Appl. Phys.* **1982**, *21*, 1569−1571.

(36) de Souza, J. P. I.; Queiroz, S. L.; Bergamaski, K.; Gonzalez, E. R.; Nart, F. C. *J. Phys. Chem. B* **2002**, *106*, 9825−9830.

(37) Jiang, L.; Colmenares, L.; Jusys, Z.; Sun, G. Q.; Behm, R. J. *Electrochim. Acta* **2007**, *53*, 377−389.

(38) Wang, H.; Jusys, Z.; Behm, R. J. *J. Power Sources* **2006**, *154*, 351−359.

(39) Alcala, R.; Mavrikakis, M.; Dumesic, J. A. *J. Catal.* **2003**, *218*, 178−190.